

This is the accepted manuscript made available via CHORUS. The article has been published as:

Tuning the band structure of graphene nanoribbons through defect-interaction-driven edge patterning

Lin Du, Tam N. Nguyen, Ari Gilman, André R. Muniz, and Dimitrios Maroudas

Phys. Rev. B **96**, 245422 — Published 22 December 2017

DOI: [10.1103/PhysRevB.96.245422](https://doi.org/10.1103/PhysRevB.96.245422)

Tuning the Band Structure of Graphene Nanoribbons through Defect-Interaction-Driven Edge Patterning

Lin Du,¹ Tam N. Nguyen,¹ Ari Gilman,¹ André R. Muniz,² and Dimitrios Maroudas^{1,*}

¹*Department of Chemical Engineering, University of Massachusetts, Amherst, Massachusetts 01003-9303, USA*

²*Department of Chemical Engineering, Federal University of Rio Grande do Sul, Porto Alegre, Rio Grande do Sul, 90040-060, Brazil*

(Dated: September 18, 2017)

We report a systematic analysis of pore-edge interactions in graphene nanoribbons (GNRs) and their outcomes based on first-principles calculations and classical molecular-dynamics simulations. We find a strong attractive interaction between nanopores and GNR edges that drives the pores to migrate toward and coalesce with the GNR edges, which can be exploited to form GNR edge patterns that impact the GNR electronic band structure and tune the GNR bandgap. Our analysis introduces a viable physical processing strategy for modifying GNR properties by combining defect engineering and thermal annealing.

I. INTRODUCTION

Graphene nanoribbons (GNRs) with widths narrower than 10 nm have outstanding electronic, thermal, and mechanical properties and are considered as very promising low-dimensional material structures for both front-end and back-end technologies in future generations of high-performance and low-power-consumption electronics¹⁻³. Although a lot of progress has been made in producing GNRs based on various physical⁴⁻⁹ or chemical¹⁰⁻¹⁴ processing techniques, fabricating GNRs narrower than 10 nm remains a challenge.

Another major challenge toward enabling the use of GNRs in future electronic device technologies is the ability to fine-tune their electronic structure for optimizing device performance. It is well known that the electronic band structure of the GNRs can be modified and their bandgap can be tuned by controlling the GNR width and edge structure^{5,15}. It has been reported that the GNR width and edge structure and morphology can be controlled in the synthesis process by choosing different molecular precursors, resulting in modifications of the GNR electronic band structure¹⁶. However, systematic physical processing strategies for precise tuning of the GNR structural and morphological features that determine their electronic structure character and control their electronic properties remain elusive.

Structural defects in graphene, generated by irradiation with electrons^{17,18} or ions^{19,20} and placed accurately at preselected positions with almost atomic precision²¹, play a key role in modifying the structure of GNRs²²⁻²⁴ and tuning their electronic properties²⁵. Real-time dynamics of defects in graphene has been recorded using aberration-corrected transmission electron microscopy²⁶. Furthermore, theoretical studies have predicted and analyzed migration of vacancies in graphene at high temperature^{22,27,28}. Thus, exploring structural modifications and systematic patterning of GNR edges, through combinations of defect engineering and thermal annealing to accelerate defect kinetics, and understanding fundamentally the resulting effects on the GNR electronic band

structure are particularly interesting and timely. In this study, based on atomic-scale calculations of pore-edge interaction energetics, we design molecular-dynamics (MD) simulations of defect dynamics near GNR edges and show how such defect-interaction-driven dynamics can be used to pattern GNR edges: such patterning introduces, in a controlled manner, GNR structural and morphological features that are capable of tuning the GNR electronic structure and properties.

II. DEFECT-ENGINEERED GNR MODEL AND COMPUTATIONAL METHODS

The simulated defect-engineered GNR is represented by a supercell with dimensions of 20 nm in the x -direction (GNR axis, with periodic boundary conditions applied in this direction) and 5-10 nm in the y -direction (GNR width), with a defect in the form of a vacancy cluster or nanopore located at the center of the supercell in the x -direction and at a varying distance, d , from a GNR edge, as shown in Fig. 1. Hydrogen or other edge-passivating atoms are not included in the supercell, as non-functionalized GNR edges can exist in vacuum²⁹, especially at high temperatures³⁰. The nanopore is constructed by removing full shells of C atoms starting from the center of a 6-member C ring; this scheme results in pore sizes of $N = 6n^2$, where n is the number of shells, yielding clusters of 6, 24, 54, 96, 150, ... C vacancies inserted in the GNR.

Pore-edge interaction energetics has been calculated in fully relaxed structures with molecular-statics (MS) computations using a conjugate-gradient algorithm. Nanopore dynamics resulting in edge patterning has been explored using molecular-dynamics (MD) simulations. In both the MS and MD simulations, the interatomic interactions were described according to the adaptive intermolecular reactive bond order (AIREBO) potential³¹, as implemented in the LAMMPS software package³². The use of the AIREBO potential in this work is justified by comparison of its pore-edge interaction energetic predic-

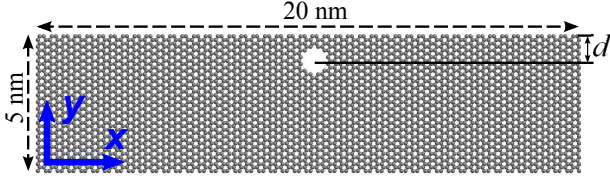


FIG. 1. Schematic representation of a simulation supercell of an armchair-edged GNR, with a 24-vacancy pore in the vicinity of the upper edge of the GNR; d is the distance between the pore's center and the GNR edge.

tions with those of first-principles density functional theory (DFT) calculations³³. In the MS computations, the simulation box size is adjusted to keep the stress equal to zero in both the x - and y -directions. To avoid interactions between periodic images, a vacuum layer with thickness of at least 20 Å in the y -direction is included in the supercell. As the distance d between the center of the pore and the GNR edge keeps increasing, the total energy of the defect-engineered GNR stops varying with d and converges to the formation energy of the nanopore in the GNR “bulk”, which provides a reference energy for reporting the pore-edge interaction energy, $U_{c-e}(d)$, corresponding to an interaction energy of 0. To accelerate the kinetics of nanopore and edge morphological dynamics and capture them within MD time scales, our MD simulations are carried out at high temperature, T , over the range 2000-3500 K, that remains significantly lower than the melting temperature of graphene³⁴. The classical equations of motion are integrated using the Verlet algorithm with a time step of 1 fs and a Nosé-Hoover thermostat and barostat is employed to control temperature at the desired level and stress at zero.

Electronic band structures of patterned GNRs are computed according to DFT within the generalized gradient approximation (GGA)³³ as implemented in the QUANTUM ESPRESSO code³⁵. The configurations used for the electronic band structure calculations were relaxed as described in Ref. 33 using a conjugate-gradient algorithm. All the computational parameters in the DFT calculations (kinetic energy cutoff, vacuum layer thickness, \mathbf{k} -point grid resolution, etc.) were determined based on systematic convergence tests of energy metrics with respect to these parameters.

III. ENERGETICS OF PORE INTERACTIONS WITH GNR EDGES

Representative AIREBO results of pore-edge interaction energetics for a 24-vacancy pore in the vicinity of an armchair-edged GNR edge are shown in Fig. 2(a), where each data point corresponds to a GNR configuration with the nanopore center at a distance d from the edge resulting in an interaction energy $U_{c-e}(d)$. It is evident that the interaction is attractive with the attraction becoming

stronger as the pore approaches very close to the edge, $d \rightarrow 0$. The inset in Fig. 2(a) is a magnification of the main plot for distances d greater than ~ 1 nm. For such a distance range, the interaction energy can be described by $U_{c-e} = A/d^\alpha$, a scaling relation similar to that for elastic cluster-sink interactions that scale like $1/d^{3/2}$. A log-log plot of $U_{c-e}(d)$ is shown in Fig. 2(b) to highlight the above scaling relation (through the excellent linear fit in the log-log plot). This scaling relation is valid over the range of pore size N that we examined. The dependence of the scaling parameters α and A on N is shown in the insets in Fig. 2(b). In general, the attractive pore-edge interaction becomes stronger with increasing pore size. These conclusions on energetics are supported by first-principles DFT calculations³³.

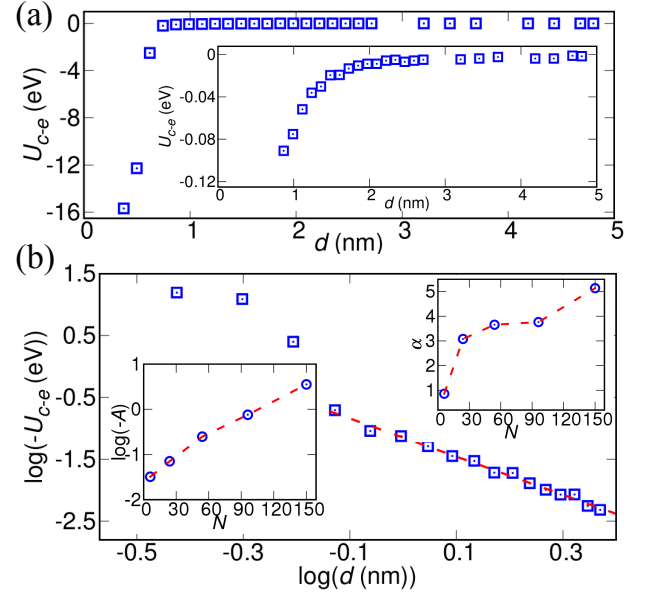


FIG. 2. (Color online) (a) Pore-edge interaction energy U_{c-e} for a 24-vacancy pore near the edge of an armchair-edged GNR as a function of the distance d between the pore center and the GNR edge. The inset is the magnification of the main plot over the range of weakly attractive interaction energies. (b) log-log plot of the pore-edge interaction energy $U_{c-e}(d)$ plotted in (a); the straight-line fit highlights the power law $U_{c-e} = A/d^\alpha$. The fitting parameters α and A are plotted as functions of pore size, N , in the insets.

IV. DYNAMICS OF DEFECT-INTERACTION-DRIVEN GNR EDGE PATTERNING

To examine the effects of the attractive interaction between the nanopore and the GNR edge on the GNR structure and edge morphology, we conducted a systematic protocol of MD simulations of pore dynamics in GNRs with pores placed in the vicinity of GNR edges, where the attractive pore-edge interaction is strong. Represen-

tative results for the dynamics of a 24-vacancy pore in the vicinity of an armchair edge of a GNR annealed at 3500 K are shown in Fig. 3. Each configuration in the sequence of Fig. 3 is mapped onto its corresponding local energy minimum. The dynamical sequence focuses on the defective region of the GNR only, while the entire simulation supercell is shown in Fig. 1.

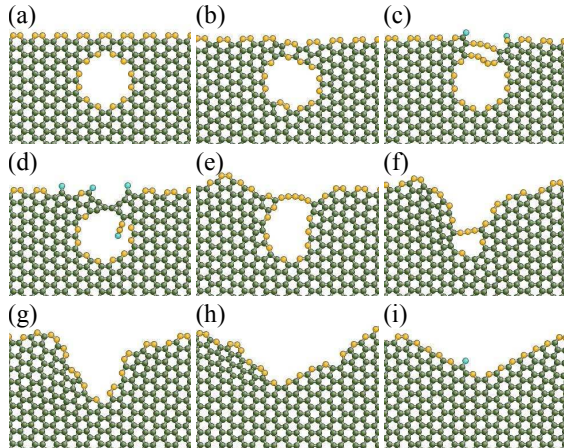


FIG. 3. (Color online) Representative quenched atomic configurations from a MD trajectory capturing the coalescence of a 24-vacancy pore with the edge of an armchair-edged GNR and the resulting edge faceting and V-shaped pattern formation at $T = 3500$ K and times of (a) 0, (b) 0.20, (c) 0.44, (d) 0.46, (e) 1.61, (f) 1.85, (g) 2.22, (h) 6.36, and (i) 12.73 ns. The atoms are colored according to their atomic coordination, Z : green, gold, and light-blue spheres represent atoms with $Z = 3, 2$, and 1 , respectively.

As seen in Fig. 3(a), the nanopore is initially very close to the armchair edge. Under the action of the attractive interaction force, the 6-membered C rings between the nanopore and the GNR edge reconstruct into the 5-7 ring defect, shown in Fig. 3(b). This is followed by the formation of a large carbon ring between the nanopore and the edge, in conjunction with the formation of two adatoms on either side of the ring, shown in Fig. 3(c). The large ring then collapses into several dangling short carbon chains, as shown in Fig. 3(d). This defective edge structure eventually evolves to form a monatomic carbon chain that separates the pore from the rest of the GNR edge. This monatomic chain migrates along the edge as shown in Fig. 3(f), until it attaches to the bottom of the edge feature corresponding to the original pore edge, completing the coalescence process of the pore with the GNR edge and forming the rough trench seen in Fig. 3(g). However, over time, this trench becomes increasingly smoother as seen in Figs. 3(h) and 3(i). The configuration of Fig. 3(i) exhibits two straight zigzag facets, *i.e.*, linear segments, in a perfect V-shaped pattern, revealing a C adatom migrating along the edge. The formation of such a GNR feature is important in terms of GNR patterning because the edge orientation plays an important role in determining the electronic structure of

the GNRs^{5,15,37,38}. The length of these zigzag facets is controlled by the size of the pore that coalesced with the armchair edge of the GNR.

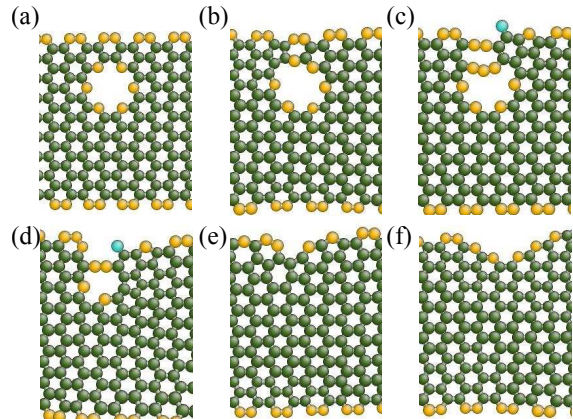


FIG. 4. (Color online) Representative quenched atomic configurations from a MD trajectory capturing the coalescence of a 6-vacancy pore with the edge of an armchair-edged GNR and the resulting edge faceting and V-shaped pattern formation at $T = 3300$ K and times of (a) 0, (b) 0.14, (c) 0.20, (d) 0.30, (e) 0.64, and (f) 3.00 ns. The atoms are colored according to their atomic coordination, Z : green, gold, and light-blue spheres represent atoms with $Z = 3, 2$, and 1 , respectively.

As mentioned above, we have conducted a systematic protocol of MD simulations over a range of pore sizes, GNR widths, and temperature, with the results of Fig. 3 being simply representative of the MD trajectories generated and the elementary kinetic steps (mechanisms) that govern the pore-edge coalescence and GNR edge patterning. These mechanisms, namely, 6-member C ring reconstruction, formation of monatomic C chain and its migration along the edge, and smoothing of the resulting rough edge morphology mediated by edge adatom diffusion leading to the formation of the V-shaped pattern, are activated when the nanopore is placed in the vicinity of the GNR edge and are identified consistently in all of our MD simulations regardless of the specific values of the simulation parameters (pore size, GNR width, etc.). This is evident in the results of Fig. 4 that shows a sequence of configurations generated by MD simulation of nanopore dynamics and GNR edge morphological evolution in the case where a smaller, 6-vacancy, pore is introduced in the vicinity of an armchair-edged GNR with width of 2.1 nm at $T = 3300$ K; note the formation of the 5-7 ring defect in Fig. 4(b) and of the migrating short monatomic C chain in Fig. 4(d). The results of Fig. 4, especially the configuration of Fig. 4(g) showing the formation of a V-shaped pattern with zigzag linear segments shorter than those of Fig. 3(i) formed by the coalescence of the 24-vacancy pore with the edge of the armchair-edged GNR, confirms that the length of the zigzag facets in the V-shaped pattern is controlled by the size of the pore placed in the vicinity of the armchair edge of the

GNR. It is also worth mentioning that, in the case of Fig. 4, in spite of the narrow width of the GNR, the interaction of the smaller nanopore with the opposite edge of the GNR is negligible compared to that with the edge near which the pore is placed and does not affect the resulting interaction-driven nanopore dynamics and GNR edge patterning.

We have constructed the minimum-energy paths (MEPs) and computed the corresponding activation energy barriers³³ for all the kinetic processes identified in the above dynamical sequence of pore migration, its coalescence with the GNR edge, and the GNR edge pattern formation using climbing-image nudged elastic band (CI-NEB) calculations³⁹. The rate-controlling energy barriers for the ring reconstruction at the initial stage of nanopore migration, the migration of the monatomic C chain, and the zigzag facet smoothening adatom migration are 3.18 eV, 2.92 eV, and 1.99 eV, respectively³³.

Transition-state theory can provide an estimation of the characteristic time scale, τ , for the completion of each one of the elementary kinetic steps discussed above and analyzed in Ref. 33, namely, ring reconstructions, monatomic C chain migration, and adatom migration on the patterned GNR edge. This time scale estimate can be expressed as $1/\tau \sim w_0 \exp[-E_a/(k_B T)]$, where w_0 is the attempt frequency (typically 10^{12} - 10^{13} s⁻¹ in crystalline solid materials), E_a is the respective energy barrier, k_B is the Boltzmann constant, and T is temperature. Using the highest energy barrier of 3.18 eV mentioned above and an attempt frequency of 5×10^{12} s⁻¹, we calculate a characteristic time scale τ for the dynamics of Fig. 3 on the order of nanoseconds, at the high annealing temperature of 3500 K, which is consistent with the time horizon of the MD simulation of Fig. 3; in general, time scales of ns to hundreds of ns are estimated for temperatures over the range of 2500-3500 K, meaning that such high temperatures can be used to capture the pore-edge coalescence processes with the resulting GNR patterning over MD time scales. Based on the above energy barriers, transition-state theory predicts a time scale on the order of seconds to hours for the above defect-interaction-driven GNR patterning over the temperature range of 1000-1250 K, *i.e.*, this patterning process can be completed within reasonable laboratory time scales at much lower temperatures than those required for realizing such kinetics in MD simulations. We also note that any kinetic mechanisms not identified at the high temperatures of the MD simulations are not expected to be activated at lower temperatures and the minimum-energy pathways of the identified kinetic mechanisms computed by the CI-NEB calculations do not change with temperature variations.

In the analysis of pore-edge interaction energetics, it was shown that increasing the pore size increases the strength of the attractive interaction and, therefore, the thermodynamic driving force for pore-edge coalescence and GNR edge patterning given by the gradient of this interaction energy. However, this does not imply that the GNR patterning process is faster for a larger pore. The

time required for the completion of this process is governed by the same elementary kinetic steps analyzed and discussed above, namely, ring reconstruction, monatomic chain migration, and adatom migration on the zigzag facets of the V-shaped features of the patterned GNR edge. It should be realized that although the respective diffusivities for these elementary kinetic steps remain practically the same at given temperature for any pore size, the corresponding diffusion lengths increase (proportionally) with increasing pore size and the times (*i.e.*, durations) for such diffusion-controlled patterning processes scale with the square of the diffusion lengths.

We conclude that our computations of interaction energetics, MD simulations of nanopore dynamics and GNR edge patterning, and time scale estimations at different annealing temperatures establish a viable physical processing strategy for patterning GNR edges. This strategy was demonstrated here through nanopore dynamics near the edge of an armchair-edged GNR, leading to formation of V-shaped edge patterns of linear zigzag segments, whose length and density can be controlled precisely by the size and density of nanopores introduced into the GNR.

V. ELECTRONIC STRUCTURE OF GNRS WITH PATTERNED EDGES

The electronic properties of GNRs with widths narrower than 10 nm depend strongly on their edge orientations. The atomic configuration and the electronic band structure of a narrow armchair-edged GNR are shown in Figs. 5(a1) and 5(b1), respectively. The band structure exhibits a bandgap of ~ 1 eV, implying a GNR with semiconducting character. However, a GNR with the same width but zigzag edges has metallic character, showing no bandgap³³. In brief, being able to manipulate the GNR edge type along the GNR edge length provides us with means to tune the electronic structure and properties of the GNRS.

In the MD simulations of Fig. 3, the length and linear density of zigzag edge segments introduced into an armchair-edged GNR can be controlled in two ways: changing the distance between neighboring nanopores, by adjusting the length of the supercell in our GNR model with the same zigzag facet pattern, as seen in Figs. 5(a2) and 5(a3), and changing the size of the nanopores, which results in different lengths of zigzag facets for the same supercell length, as seen in Figs. 5(a3)-5(a5). Through MD simulations at high temperature, we have confirmed that even very short zigzag edge segments, such as those in the configurations of Figs. 5(a2) and 5(a3) with the short V-shaped edge pattern, can be introduced into the edge of an armchair-edged GNR due to its interaction with a divacancy (pore, or vacancy cluster, with $N = 2$) placed in its vicinity.

We also mention that in our DFT calculations, we have used smaller supercells with shorter and narrower GNRS

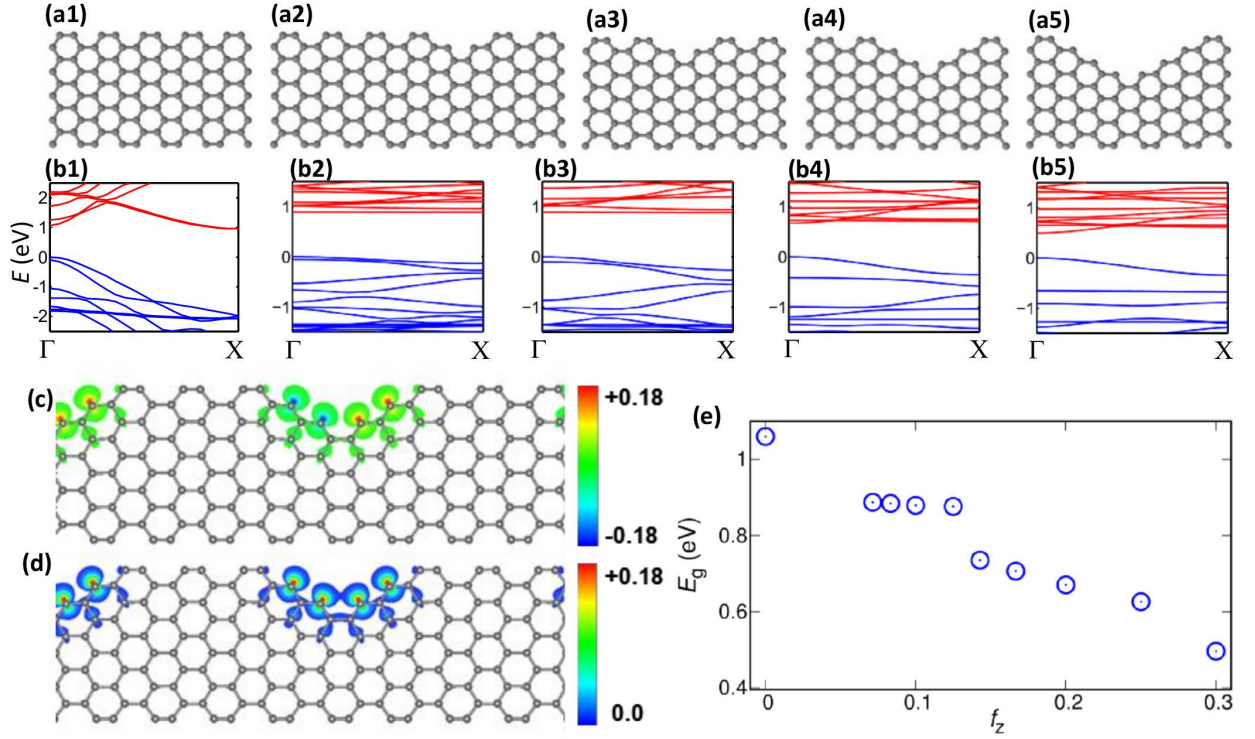


FIG. 5. (Color online) (a1-a5) Atomic structures of armchair-edged GNRs patterned with V-shaped edge features consisting of linear zigzag segments of various lengths and (b1-b5) the corresponding electronic band structures for the AFM state. Contour maps of charge density difference between spin-up and spin-down electrons ($\rho_{\text{up}} - \rho_{\text{down}}$) for the patterned GNR shown in (a4) in the (c) antiferromagnetic (AFM) and (d) ferromagnetic (FM) state. (e) Dependence of the bandgap E_g on the fraction of zigzag atoms in the patterned edges f_z .

than those studied in the MD simulations due to the substantial computational demands of the DFT calculations. In such cases, the nanopore responsible for the V-shaped patterns examined may interact with the edge of the GNR opposite to that near which the pore is placed and with the edges of neighboring pores in the periodic images of the defect-engineered GNRs. However, in all cases examined, these interactions are weaker or even negligible compared to the pore interaction with the nearby GNR edge; to within rates and durations of V-shaped pattern formation, this dominant pore-edge interaction dictates the pore dynamics and the resulting GNR patterned edge morphology.

We calculated the band structures of the patterned GNR configurations with V-shaped edge patterns with linear zigzag segments, such as those shown in Figs. 5(a2)-5(a5), using DFT calculations accounting for spin polarization. The resulting electronic band structures for the configurations of Figs. 5(a2)-5(a5) are shown in Figs. 5(b2)-5(b5), respectively. The corresponding electronic structure results based on non-spin-polarized DFT calculations are shown in Ref. 33. Specifically, based on our spin-polarized DFT calculations, we found two magnetic states, analogous to those associated with the edges of zigzag GNRs that have been reported in the literature^{15,40,41}. These studies on zigzag-edged GNRs

report the existence of a ferromagnetic (FM) state with the spins at the zigzag edges oriented along the same direction, as well as an antiferromagnetic (AFM) state with a total spin of zero, in which each edge is ferromagnetically ordered, but with opposite spin orientations on the two edges. The AFM state is the ground state, *i.e.*, it has a lower energy compared to those of the FM and non-spin-polarized states. While non-spin-polarized DFT calculations predict zigzag-edged GNRs to be metallic³³, spin-polarized DFT calculations show that zigzag-edged GNRs in the AFM state are semiconducting, with a decreasing bandgap with increasing GNR width. The origin of the bandgap in zigzag-edged GNRs has been attributed to the existence of staggered sublattice potentials resulting in magnetic ordering with opposite spin states occupying different sublattices¹⁵.

Our spin-polarized DFT calculations for our GNR structures with patterned edges predict the existence of analogous magnetic states, with the zigzag segments of the V-shaped features in the patterned armchair GNRs being ferromagnetically ordered as in the zigzag edges of zigzag-edged GNRs. In one of these states, spins in both zigzag segments of the V pattern are oriented along the same direction (FM-ordered), while in the other state, they are oriented along opposite directions (AFM-ordered). Representative charge density distri-

bution maps, corresponding to the difference between charge densities of spins paired up and down ($\rho_{\text{up}} - \rho_{\text{down}}$) are given in Figs. 5(c) and 5(d), depicting the two spin-polarized states. It is evident that the spins at the zigzag-edged segments of the V-shaped pattern are oriented in opposite directions (+ and -) in the AFM state, Fig. 5(c), while they are oriented in the same direction in the FM state, Fig. 5(d). Consistent with the zigzag-edged GNRs mentioned above, the AFM state has an energy that is lower than those of the FM and non-spin-polarized states, for all the armchair GNR configurations with V-patterned zigzag edges examined. The FM state also is more stable than the non-polarized state, implying that spin polarization helps stabilize these patterned-edge GNR configurations, in a manner analogous to that observed in zigzag-edged GNRs^{15,40,41}. Moreover, the magnetic coupling between the zigzag-edged segments with opposite spin in the AFM state stabilize the configurations further, rendering the AFM state the lowest-energy state in these patterned-edge GNR structures. These results show that the introduction of a few zigzag sites in the armchair edge is enough to introduce these states in the electronic structure (responsible for the flat conduction bands in the band structures depicted in Figs. 5(b2)-5(b5)) and reduce the bandgap. Consequently, the controlled introduction of zigzag segments into the armchair edges can be used as a strategy to tune the bandgap of the GNR.

It should be mentioned that edge defects of similar nature with the V-shaped GNR edge pattern features of the present work also have been studied broadly in the literature⁴²⁻⁴⁵, with the understanding that our work emphasizes on the formation of these GNR edge patterns as a result of pore-edge (and generally defect-edge) interactions. In particular, we mention that previous studies have also shown that an interplay of zigzag and armchair edges in GNRs may lead to significant changes in the electronic structure of the material^{37,38}.

To quantitatively analyze the dependence of the GNR bandgap on the number of “zigzag atoms” in the armchair edges, we define a metric, $f_z \equiv N_{zz}/N_{\text{tot}}$, *i.e.*, the fraction of zigzag edge atoms, where N_{zz} is the number of zigzag atoms at the GNR edge and N_{tot} is the total number of edge atoms in the supercell. The bandgap E_g of various configurations is plotted in Fig. 5(e) as a function of the zigzag edge atom fraction f_z . The upper set of points correspond to the shortest zigzag segments shown in Figs. 5(a2) and 5(a3), with different supercell lengths, showing that E_g decreases (almost linearly) with increasing f_z . A similar trend is seen for the bottom set of points which correspond to edge patterns like that of Fig. 5(a4) with varied supercell lengths. The most interesting conclusion that can be drawn from these $E_g(f_z)$ results is that the two strategies for changing the zigzag edge atom fraction, namely, changing the length of zigzag segments in the V-shaped edge pattern and changing the linear density of the V-shaped patterns, provide two scales of tuning of the GNR bandgap, a “coarse tuning” and a

“fine tuning”. Increasing the zigzag segment length can reduce the bandgap substantially, as shown by the sharp bandgap reduction between the two sets of $E_g(f_z)$ data points. However, by changing the linear density of the V-shaped patterns, the bandgap can be tuned (almost linearly) on a much finer scale, as shown within the upper and the lower sets of data points. Computational demands aside (*e.g.*, for $f_z < 0.06$), it is easy to see how the bandgap of armchair-edged GNRs can be tuned over the range from 1 eV to 0.5 eV by using these patterning strategies.

According to the electronic band structures obtained in the spin-polarized DFT calculations, such as those in Figs. 5(b2)-5(b5), the trends obtained for the dependence of the bandgap, E_g , on the fraction of zigzag sites, f_z , at the edge of the patterned GNRs are similar with those of the non-spin-polarized state³³. The spin-polarized results for $E_g(f_z)$ in Fig. 5(e) correspond to the anti-ferromagnetic (AFM) state of the patterned GNR configurations, which is energetically the most stable state. All the investigated configurations in the AFM state are semiconducting, while non-spin-polarized DFT calculations predict that the patterned-edge GNRs become metallic when f_z becomes sufficiently large³³. In other words, the qualitative trends of $E_g(f_z)$ remain the same regardless of spin polarization, although the spin-polarized configurations in the AFM state have wider bandgaps and are semiconducting. We attribute the increase in the bandgap with the inclusion of spin-polarized effects to the same reason responsible for bandgap opening in zigzag-edged GNRs discussed above¹⁵.

VI. SUMMARY AND CONCLUSIONS

In summary, we carried out a systematic analysis of pore-edge interaction energetics in GNRs and MD simulations of nanopore dynamics in the vicinity of GNR edges. We found that there is an attractive interaction between the nanopore and the GNR edge, which can drive the migration of the nanopore toward the edge and its coalescence with the edge, which is followed by the formation of a V-shaped pattern consisting of linear zigzag segments for armchair-edged GNRs. First-principles calculations based on DFT demonstrated a (almost linear) monotonic dependence of the bandgap of the patterned armchair-edged GNRs on the linear density of the zigzag edge atoms, which is tuned by controlling the size and concentration of the pores introduced in the defect-engineered GNR. Experimental verification of this physical processing strategy will establish it as a viable approach for modifying the electronic structures of GNRs synthesized in the laboratory and provide additional manufacturing flexibility for GNR patterning. The findings of this study also set the stage for future research on band structure engineering of graphene-based nanomaterials through patterning of defect-engineered graphene structures by exploiting thermodynamic driv-

ing forces due to defect interactions.

ACKNOWLEDGMENTS

This work was supported by the U.S. Department of Energy, Office of Basic Energy Sciences, Division of Materials Sciences and Engineering, under Award No. DE-FG02-07ER46407. A.R.M. also acknowledges support through Grant No. 449824/2014-4 Chamada MCTI/CNPQ/UNIVERSAL 14/2014 and computational support from CESUP/UFRGS.

-
- * Author to whom correspondence should be addressed.
Electronic mail: maroudas@ecs.umass.edu
- ¹ K. Wakabayashi, Phys. Rev. B **64**, 125428 (2001).
 - ² V. Barone, O. Hod, and G. E. Scuseria, Nano Lett. **6**, 2748 (2006).
 - ³ S. Young-Woo, M. L. Cohen, and S. G. Louie, Nature **446**, 342 (2007).
 - ⁴ Z. Chen, Y.-M. Lin, M. J. Rooks, and P. Avouris, Physica E **40**, 228 (2007).
 - ⁵ M. Y. Han, B. Özyilmaz, Y. Zhang, and P. Kim, Phys. Rev. Lett. **98**, 206805 (2007).
 - ⁶ L. Jiao, L. Zhang, X. Wang, G. Diankov, and H. Dai, Nature **458**, 877 (2009).
 - ⁷ D. V. Kosynkin, A. L. Higginbotham, A. Sinitskii, J. R. Lomeda, A. Dimiev, B. K. Price, and J. M. Tour, Nature **458**, 872 (2009).
 - ⁸ A. L. Elías, A. R. Botello-Méndez, D. Meneses-Rodríguez, V. Jehová González, D. Ramírez-González, L. Cí, E. Muñoz-Sandoval, P. M. Ajayan, H. Terrones, and M. Terrones, Nano Lett. **10**, 366 (2009).
 - ⁹ L. Jiao, X. Wang, G. Diankov, H. Wang, and H. Dai, Nat. Nanotechnol. **5**, 321 (2010).
 - ¹⁰ X. Li, X. Wang, L. Zhang, S. Lee, and H. Dai, Science **319**, 1229 (2008).
 - ¹¹ J. Cai, P. Ruffieux, R. Jaafar, M. Bieri, T. Braun, S. Blankenburg, M. Muoth, A. P. Seitsonen, M. Saleh, X. Feng, *et al.*, Nature **466**, 470 (2010).
 - ¹² S. Datta, D. R. Strachan, S. M. Khamis, and A. C. Johnson, Nano Lett. **8**, 1912 (2008).
 - ¹³ J. Campos-Delgado, J. M. Romo-Herrera, X. Jia, D. A. Cullen, H. Muramatsu, Y. A. Kim, T. Hayashi, Z. Ren, D. J. Smith, Y. Okuno, *et al.*, Nano Lett. **8**, 2773 (2008).
 - ¹⁴ X. Yang, X. Dou, A. Rouhanipour, L. Zhi, H. J. Räder, and K. Müllen, J. Am. Chem. Soc. **130**, 4216 (2008).
 - ¹⁵ Y.-W. Son, M. L. Cohen, and S. G. Louie, Phys. Rev. Lett. **97**, 216803 (2006).
 - ¹⁶ Y.-C. Chen, D. G. De Oteyza, Z. Pedramrazi, C. Chen, F. R. Fischer, and M. F. Crommie, ACS Nano **7**, 6123 (2013).
 - ¹⁷ A. Hashimoto, K. Suenaga, A. Gloter, K. Urita, and S. Iijima, Nature **430**, 870 (2004).
 - ¹⁸ M. H. Gass, U. Bangert, A. L. Bleloch, P. Wang, R. R. Nair, and A. Geim, Nat. Nanotechnol. **3**, 676 (2008).
 - ¹⁹ J.-H. Chen, W. Cullen, C. Jang, M. Fuhrer, and E. Williams, Phys. Rev. Lett. **102**, 236805 (2009).
 - ²⁰ G. Compagnini, F. Giannazzo, S. Sonde, V. Raineri, and E. Rimini, Carbon **47**, 3201 (2009).
 - ²¹ J. A. Rodriguez-Manzo and F. Banhart, Nano Lett. **9**, 2285 (2009).
 - ²² G.-D. Lee, C. Wang, E. Yoon, N.-M. Hwang, D.-Y. Kim, and K. Ho, Phys. Rev. Lett. **95**, 205501 (2005).
 - ²³ J. H. Warner, M. H. Rummeli, L. Ge, T. Gemming, B. Montanari, N. M. Harrison, B. Büchner, and G. A. D. Briggs, Nat. Nanotechnol. **4**, 500 (2009).
 - ²⁴ F. Banhart, J. Kotakoski, and A. V. Krashenninnikov, ACS Nano **5**, 26 (2010).
 - ²⁵ L. Vicarelli, S. J. Heerema, C. Dekker, and H. W. Zandbergen, ACS Nano **9**, 3428 (2015).
 - ²⁶ Ç. Ö. Girit, J. C. Meyer, R. Erni, M. D. Rossell, C. Kisielowski, L. Yang, C.-H. Park, M. Crommie, M. L. Cohen, S. G. Louie, *et al.*, Science **323**, 1705 (2009).
 - ²⁷ Y. Kim, J. Ihm, E. Yoon, and G.-D. Lee, Phys. Rev. B **84**, 075445 (2011).
 - ²⁸ J.-M. Leyssale and G. L. Vignoles, J. Phys. Chem. C **118**, 8200 (2014).
 - ²⁹ K. He, A. W. Robertson, E. Yoon, J. H. Warner, *et al.*, Nat. Commun. **5**, 3040 (2014).
 - ³⁰ G.-D. Lee, C. Wang, E. Yoon, N.-M. Hwang, and K. Ho, Phys. Rev. B **81**, 195419 (2010).
 - ³¹ S. J. Stuart, A. B. Tutein, and J. A. Harrison, J. Chem. Phys. **112**, 6472 (2000).
 - ³² S. Plimpton, J. Comput. Phys. **117**, 1 (1995).
 - ³³ See supplementary material at [URL will be provided by the publisher] for comparison of the predictions for pore-edge interaction energetics according to AIREBO and DFT, the computed MEPs of key structural transformations mediating nanopore migration and coalescence with the GNR edge and facilitating edge patterning, as well as the computed band structures for the non-spin-polarized state and ILDOSs of edge-patterned GNRs.
 - ³⁴ J. Los, K. Zakharchenko, M. Katsnelson, and A. Fasolino, Phys. Rev. B **91**, 045415 (2015).
 - ³⁵ P. Giannozzi, S. Baroni, N. Bonini, M. Calandra, R. Car, C. Cavazzoni, D. Ceresoli, G. L. Chiarotti, M. Cococcioni, I. Dabo, *et al.*, J. Phys.: Condens. Matter **21**, 395502 (2009).
 - ³⁶ L. Hu, K. D. Hammond, B. D. Wirth, and D. Maroudas, Surf. Sci. **626**, L21 (2014); S. C. Pandey, G. I. Sfyris, and D. Maroudas, Appl. Phys. Lett. **98**, 091907 (2011); L. Hu, K. D. Hammond, B. D. Wirth, and D. Maroudas, J. Appl. Phys. **115**, 173512 (2014); D. Maroudas, S. Blondel, L. Hu, K. D. Hammond, and B. D. Wirth, J. Phys.: Condens. Matter **28**, 064004 (2016).
 - ³⁷ K. Nakada, M. Fujita, G. Dresselhaus, and M. S. Dresselhaus, Phys. Rev. B **54**, 17954 (1996).
 - ³⁸ E. C. Girão, L. Liang, E. Cruz-Silva, A. G. Souza Filho, and V. Meunier, Phys. Rev. Lett. **107**, 135501 (2011).

- ³⁹ G. Henkelman, B. P. Uberuaga, and H. Jónsson, *J. Chem. Phys.* **113**, 9901 (2000).
- ⁴⁰ Y.-W. Son, M. L. Cohen, and S. G. Louie, *Nature* **444**, 347 (2006).
- ⁴¹ H. Lee, Y.-W. Son, N. Park, S. Han, and J. Yu, *Phys. Rev. B* **72**, 174431 (2005).
- ⁴² X.-J. Zhang, K.-Q. Chen, L.-M. Tang, and M.-Q. Long, *Phys. Lett. A* **375**, 3319 (2011).
- ⁴³ W. Liu, F. Meng, C. Fang, J. Zhao, J. Cheng, and X. Jiang, *Comput. Condens. Matter* **10**, 10 (2017).
- ⁴⁴ Y. Hancock, K. Saloritta, A. Uppstu, A. Harju, and M. Puska, *J. Low Temp. Phys.* **153**, 393 (2008).
- ⁴⁵ J. Baldwin and Y. Hancock, *Crystals* **3**, 38 (2013).